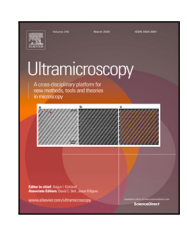


Contents lists available at ScienceDirect

### Ultramicroscopy

journal homepage: www.elsevier.com/locate/ultramic





## Quantitative magnetic mapping in TEM through accurate 2D thickness determination

Joseph Vimal Vas <sup>a</sup>, Hasan Ali <sup>a,b</sup>, Wen Shi <sup>a</sup>, Thibaud Denneulin <sup>a</sup>, Ayush K Gupta <sup>c</sup>, Rohit Medwal <sup>c</sup>, Rafal E. Dunin-Borkowski <sup>a</sup>,

- <sup>a</sup> Ernst Ruska-Centre for Microscopy and Spectroscopy with Electrons, Forschungszentrum Jülich, Jülich, 52425, Germany
- <sup>b</sup> Department of Materials Science and Engineering, Uppsala University, Uppsala, Box 534, 75121, Sweden
- <sup>c</sup> Department of Physics, Indian Institute of Technology, Kanpur, Kanpur, 52425, Uttar Pradesh, India

#### ARTICLE INFO

# Keywords: Focused ion beam Convergent Beam Electron Diffraction Electron Energy Loss Spectroscopy Electron holography Electron magnetic circular dichroism

#### ABSTRACT

Off-axis Electron Holography and Electron Magnetic Circular Dichroism are powerful Transmission Electron Microscopy (TEM) techniques capable of mapping magnetic information with near-atomic spatial resolution. However, the magnetic signals obtained is semi-quantitative due to factors such as thickness variations and local crystallographic changes. Precise determination of spatial thickness variations can make these techniques more quantitative. Electron Energy Loss Spectroscopy (EELS) provides a method to measure thickness variations within a region of interest. The absolute thickness depends on reliable estimates of the inelastic mean free path ( $\lambda$ ), which is often unknown for many materials. Alternative techniques, such as Scanning Electron Microscopy (SEM) and Convergent Beam Electron Diffraction (CBED), either lack spatial resolution in thickness mapping or are accurate only within a limited thickness range. Here, we present a straightforward approach to precisely determine the inelastic mean free path ( $\lambda$ ), enabling accurate thickness measurements from EELS maps. We compare these thickness measurements with CBED- and SEM-based methods, identifying discrepancies, particularly in thinner samples (< 100 nm). Finally, we demonstrate how this calibrated thickness measurement can provide quantitative magnetic maps using TEM-based magnetic measurements.

#### 1. Introduction

Magnetic Imaging techniques in Transmission Electron Microscopy (TEM) provide excellent spatial resolution up to atomic resolution through techniques like off-axis Electron Holography [1] and element specific mapping techniques like Electron Magnetic Circular Dichroism (EMCD) [2]. In contrast to bulk magnetic measurement techniques, the overall magnetic signal from a TEM lamella (produced from the bulk) usually depends not only on the material properties like saturation magnetization, magnetic anisotropy, Gilbert's damping factor; but also on the shape and preparation technique of the TEM lamella which introduces effects like shape anisotropy, surface amorphization etc. Some of these unknown factors, introduced primarily during sample preparation, makes the TEM based measurement techniques semiquantitative. The thickness of the samples is one such parameter which usually plays a crucial role in dictating the magnetic state of the sample [3,4] and usually needs to be accounted for while exploring effects such as spin current induced switching [5], magnetocrystalline anisotropy [6], Dzyaloshinskii-Moriya interaction (DMI) using TEM based techniques.

Focused ion beam (FIB) based sample preparation offers a versatile platform for magnetic sample preparation with controlled thickness. The TEM lamella prepared using this technique can be in the range of sub 50 nm up to 250 nm based on the application and the type of imaging to be used. The thickness control at the lower end is critical in EMCD where the signal is sensitive to sample thickness  $10-50\pm 5$  nm ([7,8]). On the other extreme, thickness upto 250 nm (or more) are required for three dimensional imaging of magnetic textures like skyrmions, chiral bobbers, magnetic hopfions and bubble ([9–12]). Understanding the spatial variation in thickness of the sample is crucial to not only segregate different magnetic contributions but also to ensure no unintended magnetic pinning sizes are created during fabrication.

Primarily, there are 3 different e-beam based methods commonly used for thickness measurements of TEM lamella - (1) scanning electron microscopy (SEM) [13], (2) electron energy loss spectroscopy (EELS) [14] and (3) convergent beam electron diffraction (CBED). Scanning electron microscope measurements involve imaging the lamella edge after the FIB sample preparation. Although this technique is convenient and has a theoretical resolution upto 0.5 nm [15], secondary

E-mail addresses: j.vas@fz-juelich.de (J.V. Vas), r.dunin-borkowski@fz-juelich.de (R.E. Dunin-Borkowski).

Corresponding authors.

electron emissions from the sample edges prevent accurate thickness determination especially for insulating samples and for thicknesses < 100 nm. Any thickness variation along the lamella cannot be accurately measured either. This method is also not convenient for conventional mechanical polishing based sample fabrication where the sample cannot be aligned edge on with the electron beam. Correlating images from different SEM detectors like through-lens detector (TLD) and the inchamber electron detector (ICE) with EELS can help extend SEM based techniques to provide Lamella site specific thickness information but this would require calibrating the EELS method first [13].

The EELS and CBED techniques are optimal for obtaining spatial variation of thickness of the TEM lamella and can be used for samples prepared with FIB and mechanical polishing. The sensitivity of the EELS technique is better for thinner samples while the CBED technique is appropriate for thicker samples. Apart from these issues, both EELS and CBED techniques require accurate estimation of the mean free path  $(\lambda)$  and extinction length  $(\xi)$  for measuring the absolute thickness. At present, there is no database or convenient method for estimating the  $\lambda$  of a custom magnetic material making absolute thickness measurements extremely difficult. The extinction length,  $\xi$  can be estimated as a fitting parameter of the CBED data but this technique offers other challenges such as sensitivity to only crystalline samples, complicated patterns in complex structures etc. A comparison between the CBED and EELS thickness showed that both the methods cover a range of thicknesses [16]. Other TEM based thickness measurements methods, based on weak beam dark field [17], geometric tilting methods [18] and High Angle Annular Dark Field Scanning TEM [19], have additional requirements such as well calibrated diffraction conditions, flat sample geometry with uniform thickness, precise tilt control, and other calibrations relative to TEM operation conditions.

The present work strives to demonstrate how an accurate thickness measurement can make magnetic imaging in TEM more quantitative. To address this problem we first determine the TEM lamella thickness using a combination of methods. Based on the error analysis, we use the best method to obtain 2D thickness of a TEM lamella. This thickness measured will then be used for magnetic measurements such as offaxis electron holography and EMCD. The manuscript consists of 3 main parts - (1) the bulk magnetic and structural characterization of the showcase magnetic material — Yttrium Iron Garnet, (2) various thickness measurement techniques on a TEM lamella and (3) magnetic measurements on YIG using Electron Holography and EMCD.

#### 2. Magnetic system and its characterization

For the present study, we use Yttrium Iron Garnet (YIG) deposited on a Gallium Gadolinium Garnet (GGG) substrate as the magnetic sample. YIG is a showcase material for developing various next-generation magnetic memory and computing architectures due to its ultralow Gilberts damping factor ( $<10^{-4}$ ). The YIG ( $10~\mu m$ )/GGG crystal used for this study was grown using liquid phase epitaxy. The quality of the bulk films were ensured using ferromagnetic resonance (FMR) measurements. The epitaxy and the chemical composition of the system were measured using scanning transmission electron microscopy (STEM) done using an FEI Titan G2 80–200 ChemiSTEM microscope with a Super-X energy dispersive X-ray spectroscopy detector operated at 200 kV and discussed in Supplementary Information, Section A. All TEM lamellae were made using the focused ion beam technique using an FEI Helios NanoLab 460F1 FIB-SEM.

#### 2.1. YIG characterization using ferromagnetic resonance (FMR)

The quality of the YIG crystal was investigated using ferromagnetic resonance (FMR) measurements with a bulk crystal of size 1 cm  $\times$  1 cm  $\times$  5 mm. Ferromagnetic resonance in YIG is excited by applying an external dc field,  $H_{dc}$  using a 3D vector magnet. The external  $H_{dc}$  exerts a torque to the magnetization of the YIG and precesses around

the  $H_{dc}$  until it damps down and aligns with the external field. In order to sustain the precession, an external ac field,  $H_{rf}$  is applied orthogonal to  $H_{dc}$  by pumping a  $I_{rf}$  into a coplanar waveguide placed beside the sample. When  $H_{rf}$  is close to the resonance frequency for a given  $H_{dc}$ , sustained oscillations of the YIG magnetization occur and are detected using field modulation technique. The FMR spectra for different frequencies in the range of 5–9 GHz were measured.

The line width,  $\Delta H$  and the resonant field,  $H_{dc}$  for different frequencies was extracted from the FMR spectra by fitting it to symmetric and asymmetric Lorentzian functions given below,

$$X(n) = L_n \frac{\Delta H (H_{dc} - H_0)}{(\Delta H)^2 + (H_{dc} - H_0)^2} + D_n \frac{(\Delta H)^2 - (H_{dc} - H_0)^2}{(\Delta H)^2 + (H_{dc} - H_0)^2}$$
(1)

The  $\Delta H$  vs. frequency curve extracted from Fig. 1a is shown in Fig. 1b. The Gibert's damping factor, $\alpha$  was extracted using a linear fit according to the equation,

$$\Delta H = \Delta H_0 + \frac{2\pi\alpha}{\gamma} f \tag{2}$$

where  $\gamma$  is the gyromagnetic ratio. The Kittel fit is shown in Fig. 1c. The in-plane anisotropy  $H_k$  and the magnetization  $M_s$  were extracted by fitting the Kittel plot to the equation,

$$f = \frac{\gamma}{2\pi} \sqrt{(H_{dc} + H_k + M_{eff})(H_{dc} + H_k)}$$
 (3)

The Gilbert's damping factor,  $\alpha$  of the YIG was estimated to be  $2.08 \times 10^{-3}$  (from Fig. 1b) while the  $M_{eff}$  and  $H_k$  was estimated to be 0.156~T and 0.0064~T (from Fig. 1c) respectively. The values of  $\alpha$  and  $M_{eff}$  are close to those reported in the literature [20,21] and thus the quality of the crystal was considered to be good. High resolution STEM imaging of the YIG and energy dispersive x-ray (EDX) spacial mapping is described in supplementary information, section A.

#### 3. Thickness measurements of TEM lamella

#### 3.1. From Electron Energy Loss Spectroscopy (EELS)

The most convenient way to measure the thickness of a TEM lamella is using electron energy loss spectroscopy. The EELS-based thickness measurement relies on the inelastic scattering of electrons as they pass through the sample. As the sample thickness increases, more electrons undergo inelastic scattering, reducing the intensity of the zero-loss peak. To obtain a spatially varying thickness map, the microscope is operated in STEM mode and the thickness of the sample is estimated from the low loss EELS spectrum. The thickness of the TEM lamella at each point of the scan is calculated from the EELS spectra using the log ratio method [22] using the formula,

$$t/\lambda = -\ln(I_0/I_t) \tag{4}$$

where  $I_0$  is the intensity of the zero loss peak and  $I_t$  is the total intensity, t is the lamella thickness at the probe position and  $\lambda$  is the inelastic mean free path in YIG. Other EELS based techniques like Bethe sum rule and Kramers-Kronig sum rule require different material parameters such as Bohr radius, number of atoms per unit area, specimen density, atomic weight, dipole polarizability per atom etc. which may be difficult to obtain for a complex material like YIG [22]. In contrast, accurately estimating thickness using the log-ratio method is only limited due to the usually unknown,  $\lambda$ , which is a property of the material and the error in measuring  $I_t$  accurately due to the energy dispersion used for the measurement.

In the present study, we measure the absolute thickness of the YIG crystal by measuring the mean free path,  $\lambda$  of YIG . The following strategy was employed for this. A cross sectional lamella of a 40 nm thick YIG grown on a GGG along the  $\langle 100 \rangle$  direction was prepared using the focused ion beam technique. A high angle annular dark field (HAADF) STEM survey image of the top interface of the lamella is shown in Fig. 2a. The  $t/\lambda$  of the thin area of YIG was measured using

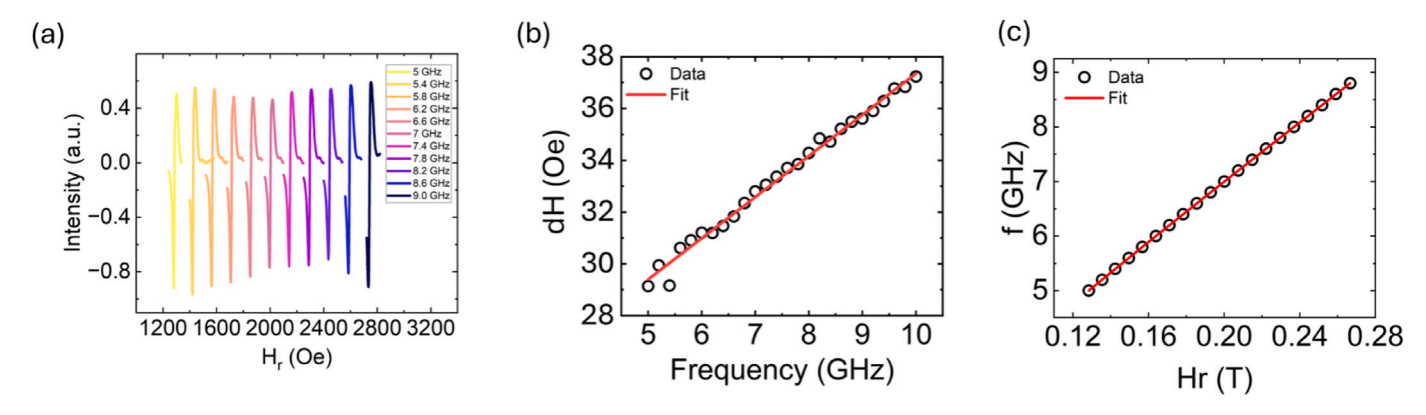


Fig. 1. Ferromagnetic resonance measurements on bulk YIG/GGG. (a) FMR spectra measured in the frequency range of 2–9 GHz, (b) linewidth vs. frequency curve and (c) Kittel plot extracted from the FMR spectra.

the Eq. (4). A representative EELS low loss spectrum is shown in Fig. 2b. A 2D low loss EELS map was acquired in the area where the 40 nm YIG is present is shown in the green box in Fig. 2a. The  $t/\lambda$  of the 40 nm YIG layer, averaged along the width of the lamella is shown in Fig. 2c. The HAADF intensity contrast is also plotted to accurately determine the region containing the YIG.

The value of the mean free path was measured by measuring the lamella thickness at the YIG area. A cross sectional lamella was made from the original lamella for this purpose. Two (10 nm) layers of gold were sputtered on either side of the lamella to create adequate Z contrast while imaging using HAADF STEM. The cross section was created by deposting adequate carbon protective layers on either side of the initial lamella by mounting it in the flip stage of the FEI Helios NanoLab 460F1 FIB-SEM. A HAADF image of the lamella is shown in Fig. 2d. The gold and the carbon layers and the YIG layer are marked in the inset of Fig. 2d (i). The sample was tilted back to the (100) zone axis using the diffraction pattern along the thickness of the YIG layer. The intensity profile of the crosssection shown in the inset of Fig. 2d provides the thickness of YIG on the initial lamella which was measured to be  $66.2 \pm 2.1$  nm. Thus, the value for the mean free path,  $\lambda$  was estimated to be 126.4  $\pm$  6.2 nm. The thickness of any YIG lamella used henceforth, can be calculated from the low loss EELS spectrum using the estimated value for  $\lambda$ . More information about the sample preparation and an EDX map of the lamella is given in supplementary information, section B. The errors in the accurate measurement of  $\lambda$ due to this method is discussed in supplementary information, section

#### 3.2. From scanning electron microscopy

The most common technique used for measuring the thickness of a TEM lamella is using the scanning electron microscope associated with the dual beam FIB. For this study, two different lamellae were produced - (1) appropriate for Electron Holography with a thickness > 100 nm and (2) for EMCD measurements with thickness < 50 nm. The SEM image of the top view and side view of both these lamella fabricated using the FIB is shown in Fig. 3a and b. The FIB fabrication was similar to the protocol employed by Tyukalova et al. [5]. Once the lamella thickness approached about 200 nm while milling at 30 kV, 80 pA, the final thinning was done at 5 kV, 40 pA. For the lamella 1 which was targetted for the EMCD studies, milling was continued until a hole developed at the bottom of the sample (the bend contours around the hole can be seen at the bottom of Fig. 3a-ii). A thickness wedge was thus created near the end of the lamella. Lamella 2 was also finished at 5 kV, 40 pA to remove the surface damage layers on either side of the lamella. The high tilt low kV milling also introduced a thickness variation near the top edge of the sample as seen in Fig. 3b-ii.

The sample thickness was measured from the SEM image of the top view of the sample as shown in Fig. 3a-i. The intensity profile along the thin area and the thick area of Lamella 1 is shown in Fig. 3c. From the top view, the thickness of the thinner area is  $57 \pm 40$  nm while the thicker area is  $424 \pm 56$  nm. The white contrast around the top of the protective layer in the SEM images, created due to large secondary electron emission near the surface, introduces uncertainty in the thickness measurement. In the thicker area, the bulk thickness is clearly visible and the uncertainty is at the edges. So the thickness was measured as the full width half maximum (FWHM) between the white contrast on either side of the edge in the green curve in Fig. 3c. For the thinner area, the top of the lamella is indistinguishable from the white contrast. The thickness was thus measured as the FWHM of the merged peak as shown in the red curve in Fig. 3c. Similar effects can be seen in lamella 2 as well and the thicknesses of the thin and thick layer was estimated to be  $208 \pm 81$  nm and  $345 \pm 60$  nm respectively.

The challenges in SEM based thickness estimation, apart from the secondary electron emission from the top, were the inability to measure local variation in thickness of the lamella, difficulty in determining appropriate beam conditions, distortions due to projection effects, getting the appropriate tilt conditions and mechanical instability when measuring features < 100 nm. From the contrast observed in Fig. 3a-ii and b-ii for lamella 1 and 2 respectively, the thickness is not uniform from top to bottom. The thickness just below the Pt layer seems to be thinner in both cases. In lamella 2, the thickness monotonically increases from this point and it is difficult to estimate the maximum thickness from the top view of the lamella 2. Similar thickness increase can be seen in lamella 1 as well. Due to the uncertainty in SEM based thickness measurements, this technique is unsuitable for quantitative magnetic analysis and was instead used as a reference for consistent lamella preparation. The secondary electron emissions from the surface can be suppressed by measuring the lamella thickness at multiple sample tilts  $> \pm 1^{\circ}$ . An example of such a measurement is discussed in supplementary information, section D. However, the error in thickness for this method remains significant.

#### 3.3. From convergent beam electron diffraction (CBED)

Thickness estimation from CBED is one of the earliest techniques developed for thickness estimation in TEM for crystalline samples since 1940s. The measurement is done in STEM mode which allows for measurement of spatial variation in sample thickness similar to EELS method. The CBED-based thickness measurement relies on dynamical electron diffraction theory. As an electron wave passes through a crystalline sample, it undergoes multiple scattering events along a given crystallographic orientation, with the scattering intensity and pattern varying as a function of thickness. The interference between the transmitted beam and the diffracted beams produces a characteristic

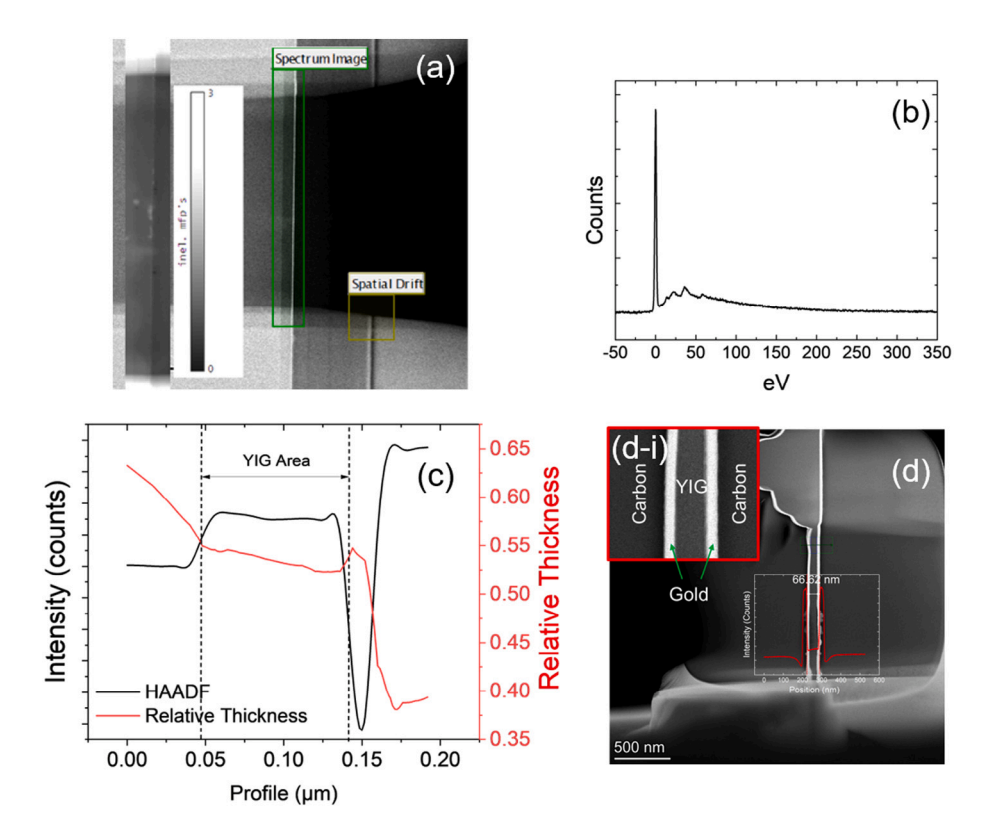


Fig. 2. Quantitative thickness measurements using EELS. (a) HAADF image of the 40 nm YIG used, (b) a sample low loss EELS spectrum, (c) profile of the  $t/\lambda$  perpendicular to the growth direction, (d) HAADF image of the cross section of the lamella showing the lamella thickness of the YIG layer, (d-i) inset showing the carbon, gold and YIG layers.

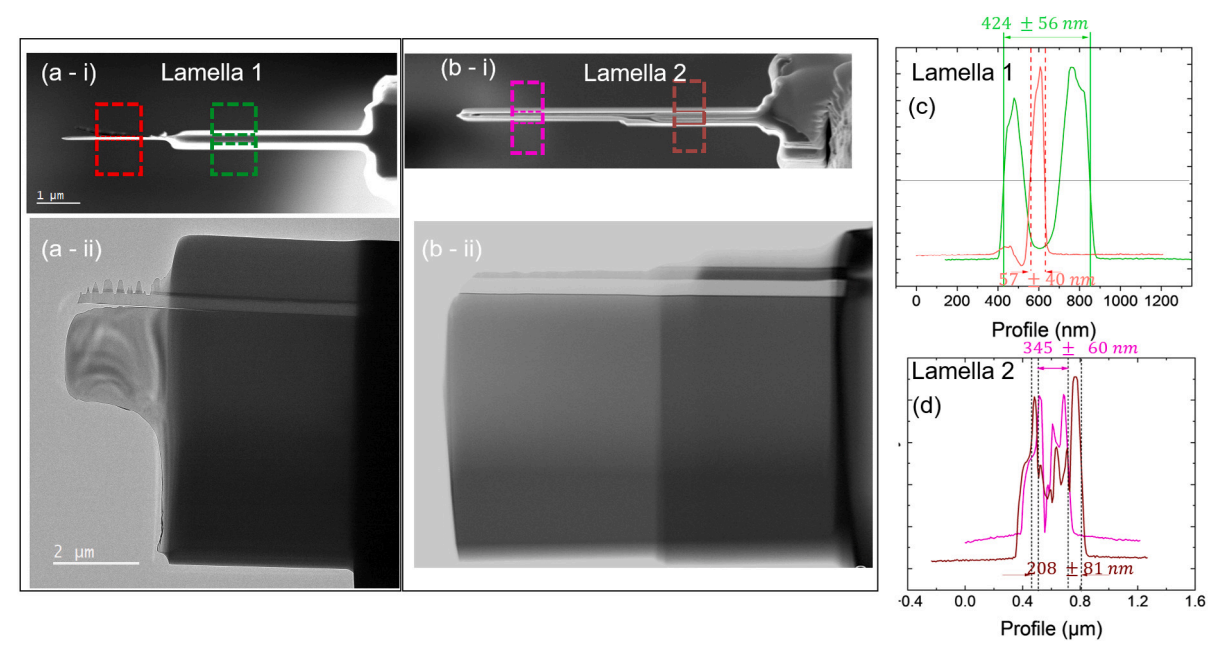


Fig. 3. SEM images of TEM lamellae used in this study, (a- i) top view and (ii) side view of TEM lamella-1 used for EMCD measurements and (b - i) top view and (ii) side view of the TEM lamella-2 used for Electron Holography, line profiles from SEM images of (c) lamella 1 and (d) lamella 2 used for measuring the sample thickness.

intensity modulation in the CBED pattern, which can be analysed to determine the sample thickness. An elaborate plotting technique for determining the thickness from CBED patterns for crystalline samples was given by [23,24]. Different computationally intensive methods for CBED based thickness measurements were demonstrated [25–27]. Even though many of these techniques can provide much more intricate

information about the crystal and accurate thicknesses. Setting up these methods is cumbersome.

In this study, the Allen and Kelly method for calculating the sample thickness from CBED technique was used. The TEM lamella used in this study was a single crystal with unit cell dimension of 12.38 Å. The YIG crystal was tilted to a 2 beam condition to observe the dark

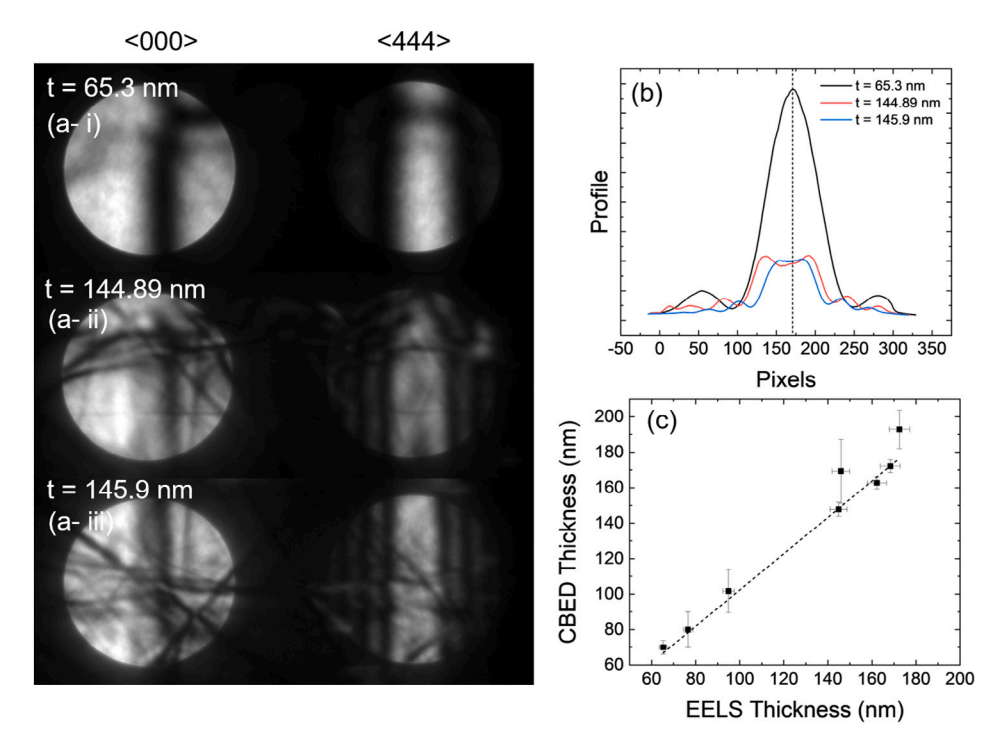


Fig. 4. (a) CBED patterns of  $\langle 000 \rangle$  and the  $\langle 4444 \rangle$  of YIG at 3 different spots with increasing thickness, (b) intensity profile of the  $\langle 4444 \rangle$  spot and (c) comparison of thickness estimated using CBED and EELS.

and bright patterns in the diffracted beam. The beam convergence is adjusted so that there is no overlap between the direct beam and the diffracted beam. For the Si samples usually used for demonstrating the CBED technique, the dark and bright bands were observed in the  $\langle 004 \rangle$ . Given the complex structure of the YIG, the  $\langle 444 \rangle$  reflection was used to obtain a similar pattern. Some representative CBED pattern obtained from YIG at various sample thickness are shown in Fig. 4a.

The Kelly and Allen methods are more straightforward and can easily be used using the software tools developed by Hou [28] which operates within the Gatan digital micrograph. The success of this method relies on finding the correct 2 beam condition which provides the expected interference pattern and chosing the right index 'n' for a given thickness range.

The fringe minima observed in the diffracted beam of the CBED is linked to the specimen thickness as per the equation,

$$(s_i^2 + 1/\xi^2)t^2 = n_i^2 \tag{5}$$

where  $s_i$  is the deviation of the *i*th minimum from the exact Bragg position,  $\xi$  is the extinction length and  $n_i$  is an integer. The  $s_i$  corresponding to each index position can be calculated from the equation,

$$s = (\Delta\theta/2\theta_B)(\lambda/d_{hkl}^2) \tag{6}$$

where  $\Delta\theta$  is the fringe position from the centre,  $2\theta_B$  is the distance in pixels between the direct beam and the diffracted beam,  $\lambda$  is the electron wavelength which is 0.02509 Å at 200 kV,  $d_{hkl}$  is the lattice spacing corresponding to the  $\langle 444 \rangle$  reflection. The thickness, t and the extinction length  $\xi$  can be extracted from the intercept and slope of a  $s_i^2/n_i^2$  vs.  $1/n_i^2$  plot as per Eq. (5). From Fig. 4a, at regions of lower thicknesses, the number of dark and bright fringes is not sufficient for calculating the sample thicknesses and thus this method is not accurate at lower than  $\approx 70$  nm lamella thickness for YIG while using the  $\langle 4444 \rangle$  reflection. The extinction length,  $\xi$  was estimated to be  $106.4 \pm 8.4$  nm. The intensity profile for various thickness of YIG are shown in Fig. 4b. Due to the large extinction length of YIG, the number of fringes available for measuring the thickness (even in thicker areas) is limited for YIG which resulted in the uncertainty in the measurements.

Table 1
Comparison between TEM lamella thickness measured using various techniques.

Points	SEM thickness (nm)	EELS thickness (nm)	CBED thickness (nm)
1.	$57 \pm 40$	$76.5 \pm 2.1$	$80 \pm 10.0$
2.	$57 \pm 40$	$94.9 \pm 2.5$	$101.7 \pm 12.2$
3.	$424 \pm 56$	$168.39 \pm 4.5$	$172.1 \pm 3.6$
4.	$424 \pm 56$	$145.48 \pm 3.9$	$169.3 \pm 1.1$
5.	$424 \pm 56$	$172.48 \pm 4.6$	$192.8 \pm 6.1$

#### 3.4. Comparison between techniques

A comparison between the different thickness measurement techniques are shown in Table 1. The measurements are done on lamella 1 shown in Fig. 3a. The first 2 measurements were done near the area marked in red while the other 3 points were made in the thicker area. For the CBED and EELS measurements, the microscope was operated in STEM mode and sample was tilted to the 2 beam condition. The camera length was adjusted to obtain the CBED pattern on the CCD camera and the spectrometer was operated such that the low loss EELS spectra could be collected if the camera is retracted. Since the CCD camera was not available with the STEM-SI mode, the beam was manually moved to collect the CBED and EELS data from the same locations on the sample. The SEM method seems to provide a thickness value considerably larger than the EELS technique and the CBED technique. This could be because of the uncertainty in the measurement introduced by secondary electron emission at both edges. The CBED thickness seems to correlate well with the EELS thickness measurements as shown in Fig. 4c. The CBED method which is more sensitive to crystalline thickness was expected to be more accurate at higher thickness range (which is reflected in the error bars) where the accuracy of the EELS method need not be accurate due to the larger scattering. No noticable effect of dead layer (created due Gallium implantation in the FIB) was visible maybe due to the large amount of low kv FIB milling used for fabricating lamella 1.

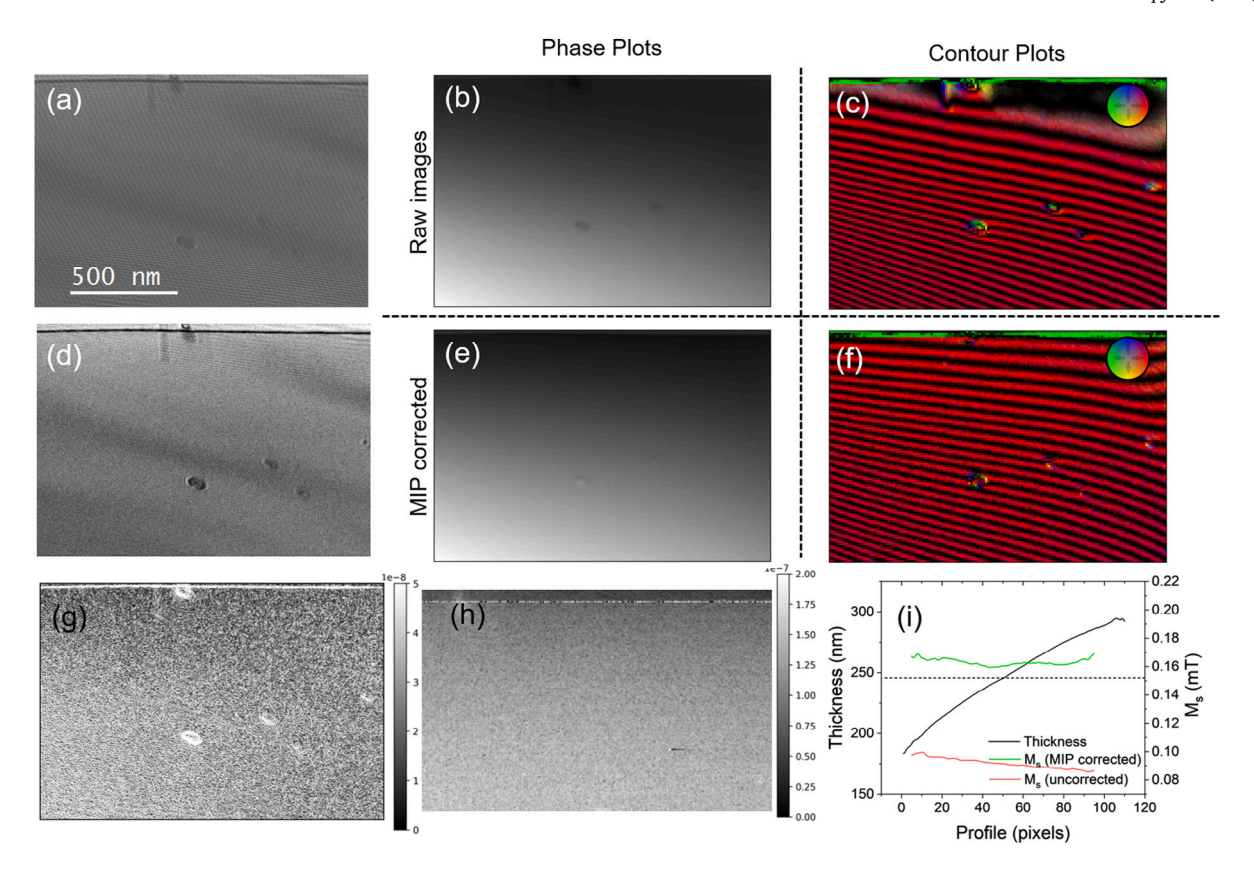


Fig. 5. Magnetization measurements using Electron Holography. (a) Hologram acquired at the top of the YIG sample, (b) phase map and (c) magnetic contour plot reconstructed from the raw hologram (d) reconstructed amplitude map. (e) phase map and (f) magnetic contour plot reconstructed after correction for mean inner potential, (g) tB calculated from the phase map, (h) thickness map of the same area measured using EELS, (i) estimated  $M_s$  with and without correction for mean inner potential.

#### 3.5. TEM-based magnetic measurements

#### 3.5.1. Off-axis electron holography

The magnetization of the YIG sample was studied using off-axis electron holography. The measurements were done on the FEI Titan G2 60–300 platform with an image corrector, a calibrated Lorentz mode and a double biprism set up. A voltage of 100 V was applied to the electron biprism and the top interface was positioned so that the beam passing through the vaccum interfered with the beam through the sample. The acquisition was done on a Gatan K2 direct electron detector for a total of 10 s. The objective lens magnetic fields and sample tilts were adjusted such that the sample was uniformly magnetized during this acquisition in-order to ensure no variation in the magnetic signal due to any domain structure near the area of interest. The hologram recorded near the top interface of the YIG sample is shown in 5a. Simultaneously a reference image was also collected in vaccum by moving the sample out of the field of view.

The reconstruction of the hologram was done using the Holoworks package version 6 [29] available in the Gatan Digital Micrograph platform. The reconstructed phase map and the amplitude map is shown in Fig. 5b and d respectively. The magnetic contour plot obtained from the raw phase is shown in Fig. 5c. In-order to obtain a pure magnetic signal, the phase contribution from the non-magnetic signal, the mean inner potential of the sample, was extracted and removed. A methodology used for the removal of MIP is given in supplementary information, section F. The phase map and the contour plot after removal of the MIP is shown in Fig. 5e and f. The YIG sample is uniformly magnetized along the x direction. The magnetic field at the top of the sample seems to be lesser than in the bulk since the density of the contour lines increases from top to bottom. This may be because of the thickness variation due to the non uniform low kv milling induced during the FIB sample preparation.

In-order to quantitatively estimate the sample magnetization, we calculate the total magnetic field encountered by the electron beam. We can calculate the tB from the electron phase difference using the equation [30,31],

$$tB = \left| \frac{\hbar}{e} [n_z \times \nabla \phi] \right| \tag{7}$$

where t is the lamella thickness, B is the magnetic field induced by the sample,  $\hbar$  is the reduced Plank's constant, e is the electron charge,  $n_z$  is the unit vector perpendicular to the sample plane and  $\phi$  is the electron phase measured in electron holography.

The reconstructed tB is shown in Fig. 5g. This magnetic field that interacts with the electron beam as it passes through the TEM lamella consists of the sample magnetization and the fringing field. Since the YIG is a soft ferromagnet, the fringing field outside the YIG is expected to be small. The direction of the fringing field is expected to be opposite on the top and bottom interfaces. Thus, the phase difference introduced is expected to be primarily due to the sample magnetization. The tB can be replaced with  $tM_s$  in Eq. (7). For a magnetic material, we do not expect the sample magnetization,  $M_s$ , (which is a material constant) to vary within the material and the observed change in intensity should be the effect of the thickness non uniformity. The thickness of the sample was measured using the EELS method in the same area so that the quantitative nature of the measurement can be ascertained. The thickness plot of the same area measured using low loss EELS is shown in Fig. 5h. The line scan comparing the thickness profile (calculated from the  $t/\lambda$ ) and the  $M_s$  calculated, with and without MIP corrected, are shown in Fig. 5i. Without MIP correction, the value of  $M_c$  was an underestimate. The  $M_s$  calculated after MIP correction correlated well with the value obtained from FMR measurements shown in Section 2.1. Thus, combining the thickness measurements using EELS along with off-axis electron holography can provide quantitative magnetic information of the YIG sample.

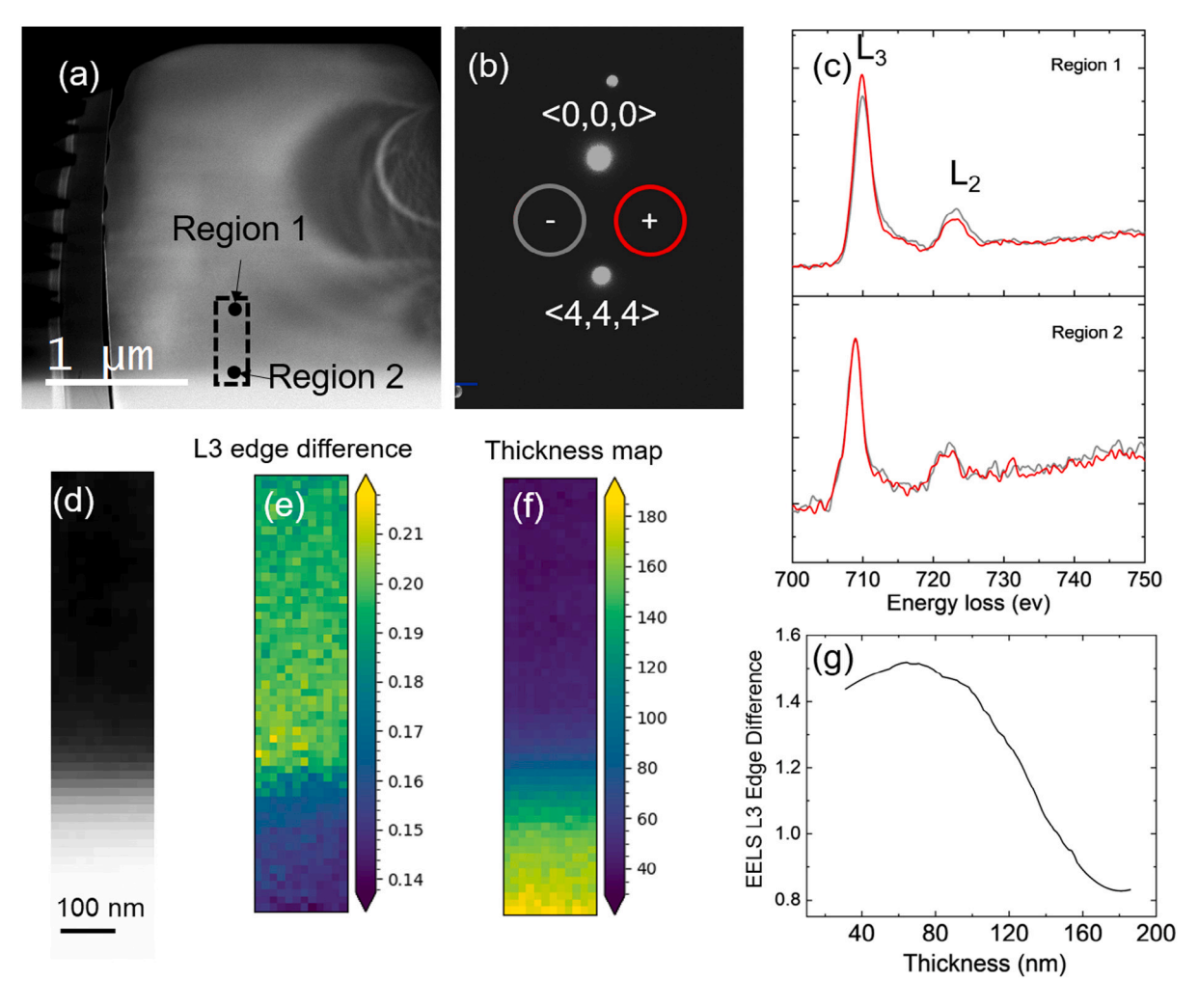


Fig. 6. EMCD signal with thickness (a) HAADF image of the sample showing the area of interest, (b) 2 beam condition showing the area used to acquire the EMCD signal, (c) EELS Fe edge after post edge normalization in a thin and thick region, (d) HAADF image of the scan area, (e) difference in L3 edge (f) Thickness map of the same area calculated from low loss EELS, (g) EELS L3 edge difference vs. thickness profile calculated from (e) and (f).

#### 3.5.2. EMCD measurements

The Fe element specific magnetic moment in YIG was mapped using the electron magnetic circular dichroism (EMCD) technique. The EMCD signal is known to be sensitive to both tilt conditions and sample thickness. In this paper, we demonstrate how the accurate thickness measurements using the EELS technique can help to choose appropriate areas of the sample for EMCD measurements. The experimental conditions for obtaining EMCD signals from YIG was demonstrated by Song et al. [32]. At 300 kV, the EMCD signal was expected when the sample thickness was between 30 and 80 nm with a 2 beam condition with the  $\langle 444 \rangle$  reflection excited. Similar conditions were used in this study for obtaining the thickness dependent EMCD signal. A YIG  $\langle 110 \rangle$  sample was cut from the bulk crystal (grown along the  $\langle 100 \rangle$  direction) using FIB to a flag geometry. The  $\langle 110 \rangle$  direction was chosen to minimize the sample tilt to approach the 2 beam condition with the  $\langle 444 \rangle$  reflection.

The EMCD experiments were carried out using a double corrected TFS spectra 300 microscope equipped with a Gatan Continuum 1066 energy filter (GIF) operated at 200 kV. The thin region achieved after the low kv milling is shown in Fig. 6a. The sample was tilted to the 2 beam condition with the  $\langle 000 \rangle$  and  $\langle 444 \rangle$  reflections as shown in Fig. 6b. For the aperture positions marked as + and – in Fig. 6b, two EELS spectra were acquired of the Fe with a dispersion of 0.25 eV/channel. The EMCD signal was recorded at the transition region between the thin and thick areas as marked in Fig. 6a. Principle

component analysis was performed on the raw signals to improve signal to noise ratio [33,34]. The EELS spectra were background subtracted and post edge normalized and their difference was taken to obtain the EMCD signal [35]. Background subtraction and post edge normalization were done to make sure that the signals captured from the two aperture positions were comparable. The peaks were also normalized at each scan position using the L3 edge obtained from the + aperture. The core loss spectrum from + and — apertures at the thinner region 1 and region 2 are shown in Fig. 6c. The EMCD signal is clearly visible in the thin region 1 on both the L3 and L2 peaks while it disappears in the thicker region 2. The HAADF image of the scanned area is shown in Fig. 6d. The difference in L3 edge indicating the EMCD signal is shown in Fig. 6e. A clear signal was observed in the thin area with the 20% difference in EMCD while the signal gradually reduced in the thick areas to below 10%. A thickness map of the same area was calculated from the calibrated low loss EELS method from the same scan area and is shown in Fig. 6e. The thickness of the sample was  $\approx 30$  nm in the thin area at the top of the scan area and can be seen gradually increasing to > 180 nm. The loss of EMCD signal matched well with the thickness map. The EMCD signal vs thickness, shown in Fig. 6g was sinusoidal in nature similar to the theoretical prediction by Song et al. [32].

The accuracy of the thickness measurements were compared using the thickness profile at region 1 and region 2. The thicknesses at regions 1 and 2 were 76 nm and 145.5 nm according to calibrated

EELS compared to 118 nm and 157.5 nm as measured using CBED. The EMCD signal was expected to be observed in the thickness range of 30 to 80 nm. Given the signals observed in Fig. 6c, the thickness measured by calibrated EELS seems to be much more accurate as compared to CBED.

#### 4. Conclusions

The influence of TEM lamella thickness towards quantitative magnetic mapping using off-axis electron holography and electron magnetic circular dichroism was investigated. The sample system used for this study was Yttrium Iron Garnet, a ferrimagnetic insulator. Three commonly used thickness measurement techniques — SEM based, EELS based and CBED based, were investigated for accurately determining the 2D thickness of a TEM lamella. An experimental strategy to accurately calibrate the inelastic mean free path,  $\lambda$ , in low loss EELS based thickness measurements was pursued to obtain absolute thickness values from this technique. For the YIG sample, the inelastic mean free path,  $\lambda$ , was measured to be 126.4  $\pm$  6.2 nm. The SEM based technique had larger errors associated with it. The CBED technique correlated well with the EELS measurements. The absolute thickness values obtained from the EELS technique were used to quantify the magnetic signal measured using electron holography. After correcting for the mean inner potential, the  $M_s$  measured from electron holography, showed good agreement with bulk FMR measurements. The thickness vs. EELS signal followed the theoretically predictions. From the calibrated EMCD measurements, the dependence on the sample thickness (in the 40-120 nm) on the L3 edge difference is clearly visible.

#### CRediT authorship contribution statement

Joseph Vimal Vas: Writing – original draft, Visualization, Validation, Methodology, Investigation, Formal analysis, Data curation, Conceptualization. Hasan Ali: Writing – original draft, Supervision, Software, Funding acquisition, Formal analysis, Data curation, Conceptualization. Wen Shi: Investigation. Thibaud Denneulin: Methodology, Investigation, Formal analysis, Data curation. Ayush K Gupta: Formal analysis, Data curation. Rohit Medwal: Writing – original draft, Funding acquisition, Data curation, Conceptualization. Rafal E. Dunin-Borkowski: Validation, Supervision, Funding acquisition.

#### **Declaration of competing interest**

The authors declare that they have no known competing financial interests or personal relationships that could have appeared to influence the work reported in this paper.

#### Acknowledgements

R. D. B. acknowledges the financial support from the European Research Council under the European Union's Horizon 2020 Research and Innovation Programme (grant 856538; project '3D MAGiC'). H.A. acknowledges the financial support by Swedish Research Council (project no. 2021-06748). R. M. acknowledges the financial support by I-HUB Quantum Technology Foundation (project no. 2023288). A.K.G. would like to acknowledge Ministry of Education, Government of India for financial support through Prime Minister's Research Fellowship (PMRF).

#### Appendix A. Supplementary data

Supplementary material related to this article can be found online at https://doi.org/10.1016/j.ultramic.2025.114140.

#### Data availability

Data will be made available on request.

#### References

- [1] F. Winkler, J. Barthel, A.H. Tavabi, S. Borghardt, B.E. Kardynal, R.E. Dunin-Borkowski, Absolute scale quantitative off-axis electron holography at atomic resolution, Phys. Rev. Lett. 120 (15) (2018) 156101, http://dx.doi.org/10.1103/PhysRevLett.120.156101, [Online]. Available: https://link.aps.org/doi/10.1103/PhysRevLett.120.156101, Publisher: American Physical Society.
- [2] J. Rusz, S. Muto, J. Spiegelberg, R. Adam, K. Tatsumi, D.E. Bürgler, P.M. Oppeneer, C.M. Schneider, Magnetic measurements with atomic-plane resolution, Nat. Commun. 7 (1) (2016) 12672, http://dx.doi.org/10.1038/ncomms12672, [Online]. Available: https://www.nature.com/articles/ncomms12672, Publisher: Nature Publishing Group.
- [3] K. Shibata, A. Kovács, N.S. Kiselev, N. Kanazawa, R.E. Dunin-Borkowski, Y. Tokura, Temperature and magnetic field dependence of the Internal and Lattice structures of skyrmions by Off-Axis electron holography, Phys. Rev. Lett. 118 (8) (2017) 087202, http://dx.doi.org/10.1103/PhysRevLett.118.087202, [Online]. Available: https://link.aps.org/doi/10.1103/PhysRevLett.118.087202, Publisher: American Physical Society.
- [4] H.S. Park, X. Yu, S. Aizawa, T. Tanigaki, T. Akashi, Y. Takahashi, T. Matsuda, N. Kanazawa, Y. Onose, D. Shindo, A. Tonomura, Y. Tokura, Observation of the magnetic flux and three-dimensional structure of skyrmion lattices by electron holography, Nature Nanotechnology 9 (5) (2014) 337–342, http://dx.doi.org/10.1038/nnano.2014.52, [Online]. Available: https://www.nature.com/articles/nnano.2014.52, Publisher: Nature Publishing Group.
- [5] E. Tyukalova, J. Vimal Vas, R. Ignatans, A.D. Mueller, R. Medwal, M. Imamura, H. Asada, Y. Fukuma, R.S. Rawat, V. Tileli, M. Duchamp, Challenges and applications to operando and in situ TEM imaging and spectroscopic capabilities in a cryogenic temperature range, Acc. Chem. Res. 54 (16) (2021) 3125–3135, http://dx.doi.org/10.1021/acs.accounts.1c00078, [Online]. Available: https://doi.org/10.1021/acs.accounts.1c00078, Publisher: American Chemical Society.
- [6] C. Beeli, B. Doudin, J.P. Ansermet, P. Stadelmann, Off-axis electron holography of single ferromagnetic nanowires, Mater. Charact. 42 (4) (1999) 175–182, http://dx.doi.org/10.1016/S1044-5803(99)00012-1, [Online]. Available: https://www.sciencedirect.com/science/article/pii/S1044580399000121.
- [7] H. Ali, S.K.M. Sathyanath, C.-W. Tai, J. Rusz, T. Uusimaki, B. Hjörvarsson, T. Thersleff, K. Leifer, Single scan STEM-EMCD in 3-beam orientation using a quadruple aperture, Ultramicroscopy 251 (2023) 113760, http://dx.doi.org/10.1016/j.ultramic.2023.113760, [Online]. Available: https://www.sciencedirect.com/science/article/pii/S0304399123000773.
- [8] H. Ali, J. Rusz, T. Warnatz, B. Hjörvarsson, K. Leifer, Simultaneous mapping of EMCD signals and crystal orientations in a transmission electron microscope, Sci. Rep. 11 (1) (2021) 2180, http://dx.doi.org/10.1038/s41598-021-81071-4, [Online]. Available: https://www.nature.com/articles/s41598-021-81071-4, Publisher: Nature Publishing Group.
- [9] F. Zheng, N.S. Kiselev, F.N. Rybakov, L. Yang, W. Shi, S. Blügel,
   R.E. Dunin-Borkowski, Hopfion rings in a cubic chiral magnet, Nature
   623 (7988) (2023) 718–723, http://dx.doi.org/10.1038/s41586-023-06658-5,
   [Online]. Available: https://www.nature.com/articles/s41586-023-06658-5,
   Publisher: Nature Publishing Group.
- [10] D. Kong, A. Kovács, M. Charilaou, F. Zheng, L. Wang, X. Han, R.E. Dunin-Borkowski, Direct observation of tensile-strain-induced nanoscale magnetic hardening, Nat. Commun. 14 (1) (2023) 3963, http://dx.doi.org/10.1038/s41467-023-39650-8, [Online]. Available: https://www.nature.com/articles/s41467-023-39650-8, Publisher: Nature Publishing Group.
- [11] Y. He, T. Helm, I. Soldatov, S. Schneider, D. Pohl, A.K. Srivastava, A.K. Sharma, J. Kroder, W. Schnelle, R. Schaefer, B. Rellinghaus, G.H. Fecher, S.S.P. Parkin, C. Felser, Nanoscale magnetic bubbles in \${\mathrm{nd}}\_{2}{{2}{{\mathbf o} (2022) 064426, http://dx.doi.org/10.1103/PhysRevB.105. 064426, [Online]. Available: https://link.aps.org/doi/10.1103/PhysRevB.105. 064426, Publisher: American Physical Society.
- [12] F. Zheng, F.N. Rybakov, A.B. Borisov, D. Song, S. Wang, Z.-A. Li, H. Du, N.S. Kiselev, J. Caron, A. Kovács, M. Tian, Y. Zhang, S. Blügel, R.E. Dunin-Borkowski, Experimental observation of chiral magnetic bobbers in B20-type FeGe, Nature Nanotechnology 13 (6) (2018) 451–455, http://dx.doi.org/10.1038/s41565-018-0093-3, [Online]. Available: https://www.nature.com/articles/s41565-018-0093-3, Publisher: Nature Publishing Group.
- [13] A. Conlan, E. Tillotson, A. Rakowski, D. Cooper, S. Haigh, Direct measurement of TEM lamella thickness in FIB-SEM, J. Microsc. 279 (3) (2020) 168–176, http://dx.doi.org/10.1111/jmi.12852, [Online]. Available: https://onlinelibrary. wiley.com/doi/abs/10.1111/jmi.12852, \_eprint: https://onlinelibrary.wiley.com/ doi/odf/10.1111/jmi.12852.
- [14] T. Malis, S.C. Cheng, R.F. Egerton, EELS log-ratio technique for specimen-thickness measurement in the TEM, J. Electron Microsc. Tech. 8 (2) (1988) 193–200, http://dx.doi.org/10.1002/jemt.1060080206, [Online]. Available: https://onlinelibrary.wiley.com/doi/abs/10.1002/jemt.1060080206, \_eprint: https://onlinelibrary.wiley.com/doi/pdf/10.1002/jemt.1060080206.
- [15] A.E. Vladár, K.T. Arat, Limits of resolutions in the scanning electron microscope, Microsc. Microanal. 29 (2023) 463–464, http://dx.doi.org/10.1093/micmic/ ozad067.218.

- [16] Y.-U. Heo, Comparative study on the specimen thickness measurement using EELS and CBED methods, Appl. Microsc. 50 (1) (2020) 8, http://dx.doi.org/10. 1186/s42649-020-00029-4.
- [17] D.B. Williams, C.B. Carter, Weak-beam dark-field microscopy, in: D.B. Williams, C.B. Carter (Eds.), Transmission Electron Microscopy: A Textbook for Materials Science, Springer US, 1996, pp. 421–438, http://dx.doi.org/10.1007/978-1-4757-2519-3 26.
- [18] J.-H. Lee, H. Suh, S.-G. Lee, J.-G. Kim, S.J. Yoo, Advanced method for the accurate measurement of tilt angle in a transmission electron microscopy goniometer, J. Anal. Sci. Technol. 9 (1) (2018) 6, http://dx.doi.org/10.1186/s40543-018-0140-6
- [19] H. Nukala, Quantitative thickness mapping in high-angle annular dark-field (haadf) scanning transmission electron microscopy (stem), 2008, [Online]. Available: https://stars.library.ucf.edu/etd/3670.
- [20] L. Soumah, N. Beaulieu, L. Qassym, C. Carrétéro, E. Jacquet, R. Lebourgeois, J. Ben Youssef, P. Bortolotti, V. Cros, A. Anane, Ultra-low damping insulating magnetic thin films get perpendicular, Nat. Commun. 9 (1) (2018) 3355, http://dx.doi.org/10.1038/s41467-018-05732-1, [Online]. Available: https://www.nature.com/articles/s41467-018-05732-1, Publisher: Nature Publishing Group.
- [21] R. Medwal, U. Chaudhuri, J.V. Vas, A. Deka, S. Gupta, M. Duchamp, H. Asada, Y. Fukuma, R. Mahendiran, R.S. Rawat, Magnetoimpedance of epitaxial Y3Fe5012 (001) thin film in low-frequency regime, ACS Appl. Mater. Interfaces 12 (37) (2020) 41802–41809, http://dx.doi.org/10.1021/acsami.0c13213, [Online]. Available: https://doi.org/10.1021/acsami.0c13213, Publisher: American Chemical Society.
- [22] R. Egerton, S. Cheng, Measurement of local thickness by electron energy-loss spectroscopy, Ultramicroscopy 21 (3) (1987) 231–244, http://dx.doi.org/10.1016/0304-3991(87)90148-3, [Online]. Available: https://www.sciencedirect.com/science/article/pii/0304399187901483.
- [23] P.M. Kelly, A. Jostsons, R.G. Blake, J.G. Napier, The determination of foil thickness by scanning transmission electron microscopy, Phys. Status Solidi ( A) 31 (2) (1975) 771–780, [Online]. Available: https://onlinelibrary.wiley.com/ doi/abs/10.1002/pssa.2210310251, Publisher: John Wiley & Sons, Ltd.
- [24] S.M. Allen, Foil thickness measurements from convergent-beam diffraction patterns, Phil. Mag. A 43 (2) (1981) 325–335, http://dx.doi.org/10.1080/ 01418618108239412, Publisher: Taylor & Francis \_eprint: https://doi.org/10. 1080/01418618108239412.
- [25] M. Klinger, M. Němec, L. Polívka, V. Gärtnerová, A. Jäger, Automated CBED processing: Sample thickness estimation based on analysis of zone-axis CBED pattern, Ultramicroscopy 150 (2015) 88–95, http://dx.doi.org/10.1016/j.ultramic.2014. 12.006, [Online]. Available: https://www.sciencedirect.com/science/article/pii/S0304399114002575.
- [26] S. Honglong, L. Minting, W. Wenzhong, CBED Tools for semi-automatic measurement of crystal thicknesses, J. Appl. Crystallogr. 50 (1) (2017) 313–319, http://dx.doi.org/10.1107/S1600576716019476, [Online]. Available: https://scripts.iucr.org/cgi-bin/paper?S1600576716019476.

- [27] D. Delille, R. Pantel, E. Van Cappellen, Crystal thickness and extinction distance determination using energy filtered CBED pattern intensity measurement and dynamical diffraction theory fitting, Ultramicroscopy 87 (1) (2001) 5–18, http:// dx.doi.org/10.1016/S0304-3991(00)00067-X, [Online]. Available: https://www. sciencedirect.com/science/article/pii/S030439910000067X.
- [28] V. Hou, A DigitalMicrograph™ script for crystal thickness measurements using convergent beam electron diffraction, Microsc. Microanal. 10 (2004) 1380–1381, http://dx.doi.org/10.1017/S1431927604881637, [Online]. Available: https://www.cambridge.org/core/journals/microscopy-and-microanalysis/article/abs/digitalmicrograph-script-for-crystal-thickness-measurements-using-convergent-beam-electron-diffraction/07A33F53C6A229033BF40E4E8AB1A52F.
- [29] E. Völkl, L.F. Allard, B. Frost, A software package for the processing and reconstruction of electron holograms, J. Microsc. 180 (1) (1995) 39–50, [Online]. Available: https://onlinelibrary.wiley.com/doi/abs/10.1111/j.1365-2818. 1995.tb03655.x, Publisher: John Wiley & Sons, Ltd.
- [30] V.V. Volkov, Y. Zhu, Lorentz phase microscopy of magnetic materials, Ultramicroscopy 98 (2) (2004) 271–281, http://dx.doi.org/10.1016/j.ultramic.2003. 08.026, [Online]. Available: https://www.sciencedirect.com/science/article/pii/ S0304399103002079.
- [31] F.A.M. Ramirez, T. Kasama, R.E. Dunin-Borkowski, M. Beleggia, Holography Different fields of application, in: Holography Different Fields of Application, IntechOpen, 2011, http://dx.doi.org/10.5772/750, [Online]. Available: https://www.intechopen.com/chapters/undefined/chapters/19623.
- [32] D. Song, G. Li, J. Cai, J. Zhu, A general way for quantitative magnetic measurement by transmitted electrons, Sci. Rep. 6 (1) (2016) 18489, http: //dx.doi.org/10.1038/srep18489, [Online]. Available: https://www.nature.com/ articles/srep18489, Publisher: Nature Publishing Group.
- [33] J. Spiegelberg, J. Rusz, Can we use PCA to detect small signals in noisy data? Ultramicroscopy 172 (2017) 40–46, http://dx.doi.org/10.1016/j.ultramic.2016. 10.008, [Online]. Available: https://www.sciencedirect.com/science/article/pii/S0304399116302480.
- [34] P. Trebbia, N. Bonnet, EELS elemental mapping with unconventional methods I. Theoretical basis: Image analysis with multivariate statistics and entropy concepts, Ultramicroscopy 34 (3) (1990) 165–178, http://dx.doi.org/10.1016/0304-3991(90)90070-3, [Online]. Available: https://www.sciencedirect.com/science/article/pii/0304399190900703.
- [35] H. Ali, T. Warnatz, L. Xie, B. Hjörvarsson, K. Leifer, Quantitative EMCD by use of a double aperture for simultaneous acquisition of EELS, Ultramicroscopy 196 (2019) 192–196, http://dx.doi.org/10.1016/j.ultramic.2018. 10.012, [Online]. Available: https://www.sciencedirect.com/science/article/pii/S0304399118302821.